LDA + U_{sc} calculations of phase relations in FeO

Yang Sun,[1] Matteo Cococcioni,[2] and Renata M. Wentzcovitch[1,3,4,*]

[1]*Department of Applied Physics and Applied Mathematics, Columbia University, New York, New York 10027, USA*

[2]*Department of Physics, University of Pavia, 27100 Pavia, Italy*

[3]*Department of Earth and Environmental Sciences, Columbia University, New York, New York 10027, USA*

[4]*Lamont–Doherty Earth Observatory, Columbia University, Palisades, New York 10964, USA*

(Received 31 March 2020; accepted 27 May 2020; published 9 June 2020)

Using the LDA + U_{sc} method, we present calculation phase relations of iron monoxides involving five polytypes in multiple spin-state configurations. The Hubbard parameter U is determined self-consistently simultaneously with the occupation matrix and structures at arbitrary pressures. The Hubbard parameter strongly depends on pressure, structure, and spin state. Comparison with experimental structural data indicates the LDA + U_{sc} can predict structure, compression curves, phase relations, and transition pressures very well for the insulating $B1$ and $iB8$ states. However, it requires additional calculations using the Mermin functional that includes the electronic entropic contribution to the free energy to obtain an $nB8$ metallic state and a consistent $iB8$ to $nB8$ insulator to metal transition pressure.

DOI: 10.1103/PhysRevMaterials.4.063605

I. INTRODUCTION

Fe-O is one of the most fundamental components of the Earth's mantle and possibly also of the Earth's core. Phase relations in FeO are essential to determining the state of iron at the extreme pressures of deep planetary environments. Several challenging experiments under extreme conditions have been performed in FeO in the last decades [1–6]. FeO is also an archetypical strongly correlated material [7]. From the materials simulations viewpoint, it is an important test case in the development of methods to predict phase stability at arbitrary conditions.

Modern computational materials discovery methods have shown to be an ideal tool to discover new materials at extreme conditions [8,9]. However, these methods have achieved only limited success for the Fe-O system [10–12]. With few exceptions [6], they mostly predicted phases that are not observed experimentally. The presence of localized and strongly correlated *3d* electrons in iron prevents successful applications of *ab initio* methods using conventional exchange-correlation functionals such as the local-density approximation (LDA) or the generalized gradient approximation (GGA) to the Fe-O system. For example, it is a well-known fact that conventional band-structure calculations with the LDA or GGA incorrectly give a metallic ground state for FeO in the B1 structure. This problem has been solved by using many-body electronic structure methods that address the strongly correlated state of the *3d* electrons [13–17]. For example, by including the Hubbard correction in these standard density-functional theory (DFT) calculations, DFT+U calculations open the Hubbard gap and produce the insulating state of $B1$-type FeO [13,18]. The reliability of the DFT+U results depends on the Hubbard parameter U. While it has been argued that U should be determined by first principles [14], self-consistently [19], and be structure- and spin-state dependent [20–24], many studies have employed a constant and semiarbitrary U value or tuned U to match experimental observations of some sort. While useful in providing insights into the electronic structure problem (see, e.g., Refs. [25,26]), these calculations have not fully explored the predictive power of this method. The full dependence of U on pressure/volume, structure, spin state, chemistry, etc., must be computed if one is to make predictions at extreme conditions in the presence of dissociation or recombination reactions. On the other hand, determining the Hubbard parameter is a nontrivial task [14,19]. Still, a recent implementation based on density-functional perturbation theory (DFPT) and monochromatic perturbations [27] dramatically facilitates the calculation of U by decreasing the computational effort by orders of magnitude.

In this work, we focus on the iron monoxide, which is the most frequently studied of the Fe-O compounds. We consider iron monoxide in five polytypes and investigate the predictive power of self-consistent LDA + U_{sc} calculations to reproduce its experimental phase relations. We compute relative phase stabilities, equations of state, and transition pressures, and compare them with experimental information.

In the next section, we review previous high-pressure works on iron monoxide. Section III discusses the methods used to compute the Hubbard U and total energies while Sec. IV presents and discusses our results. Conclusions are presented in Sec. V.

II. REVIEW OF PREVIOUS WORKS

FeO has a complex phase diagram. At ambient conditions, FeO forms a cubic NaCl-type $B1$ structure. At higher pressure or lower temperature, the symmetry reduces to rhombohedral ($rB1$) with antiferromagnetic ordering along [111] [1]. The phase boundary between the $B1$ and $rB1$ was measured at and

*rmw2150@columbia.edu

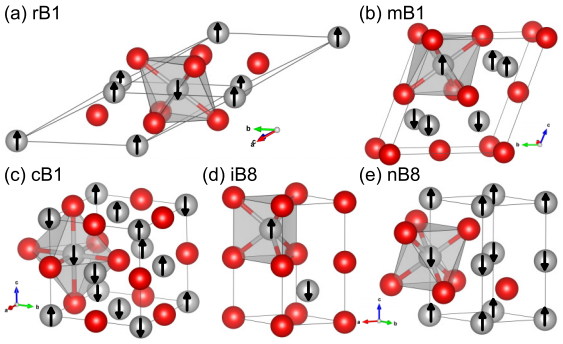

FIG. 1. Crystal structures and magnetic configurations for (a) rhombohedral $B1$, (b) monoclinic $B1$, (c) cubic $B1$ phases, (d) inverse $B8$, and (e) normal $B8$. Iron is shown in gray and oxygen in red. Arrows indicate the spin orientation. The iron coordination number is indicated by the surrounding polyhedron.

above room temperature [2,28,29]. While the $rB1$ phase is usually considered to be the ground state at low temperatures up to ∼100 GPa [30], Fjellvag *et al.* [31] observed further symmetry reduction from rhombohedral to monoclinic at $T =$ 10 K. This lower symmetry also features a local Jahn-Teller distortion of FeO_6 octahedron that produces four short and two long bonds [31]. With DFT+U calculations, Cococcioni and de Gironcoli [14] described the reduced symmetry of the rhombohedral lattice by moving the minority-spin d electron from the $a_{1g}(z^2)$ orbital to one of the degenerate t_{2g} orbitals. Gramsch *et al.* [25] explained the monoclinic symmetry could lead to the splitting of the e_g pair into a_g and b_g states and the a_g orbital occupancy could be stabilized by the Hubbard parameter. However, phase stability and phase transitions in the monoclinic phase were not addressed in these studies.

Fei and Mao found experimentally that under pressure, the $rB1$ phase transforms to the $B8$ phase above 90 GPa at 600 K [2]. The equilibrium phase boundary between $rB1$ and $B8$ was found near 105 GPa at room temperature [30,32]. Two polytypes of $B8$ FeO have been reported [28,33,34]: (a) the normal NiAs-type $B8$ structure ($nB8$ hereafter) and (b) the inverse $B8$ structure ($iB8$ hereafter). The main structural difference between $nB8$ and $iB8$ phases is that the Fe and O positions are swapped. These structures have different Fe coordination polyhedra. In the $iB8$ structure, the coordination polyhedron is a triangular prism, while in the $nB8$ structure it is an octahedron (see Fig. 1). A high-spin (HS) to low-spin (LS) state change was also found in FeO at high pressures. This transition pressure has been debated for a long time. Pasternak *et al.* suggested that the HS state transforms into the LS state at 90 GPa [35]. Later, Badro *et al.* [36] reported the HS could be preserved up to 143 GPa at room temperature. Mattila *et al.* [37] found that LS FeO existed above 140 GPa. Most recently, Ohta *et al.* demonstrated that the structural transition from $iB8$ to $nB8$, as well as the HS-LS state change and the insulator-metal transition, all happened concurrently near 120 GPa with little temperature dependence [38,39].

Theoretical calculations by Sherman and Jansen [40] reported a structural transition from $rB1$ to $B8$ at 130 GPa using the LDA. Cohen *et al.* [3] found the magnetic collapse in the $B1$ structure at 100 GPa with LDA or at 200 GPa with GGA. Mazin [33] indicated that the GGA and LDA exchange-correlation functionals *could not* describe the relative stability between $iB8$ and $nB8$. Persson *et al.* [26] obtained the spin-state change in $B1$ near 200 GPa using GGA+U with constant U (3 and 5 eV). The metal-insulator transitions (MIT) of FeO were mainly studied by the combination of DFT and dynamical mean-field theory (DFT+DMFT). Shorikov *et al.* [16] predicted the MIT for $B1$-HS at 60GPa at room temperature. The prediction does not agree with experiments [29]. Later, Ohta *et al.* performed DFT+DMFT calculations for the $B1$ phase and obtained results consistent with experimental observations that the $B1$ phase metallization happened at high temperature and high pressure, and it was related to the HS-LS transition [29]. Leonov [41] also showed that DFT+DMFT could describe the MIT for the B1 phase and that the transition pressure changed with the Hubbard parameter.

III. METHODS

Here, DFT+U calculations were performed using the simplified formulation of Dudarev *et al.* [42] as implemented in the QUANTUM ESPRESSO code [43,44]. The LDA was used for the exchange-correlation functional. We have used ultrasoft pseudopotentials [45] with valence electronic configurations $3s^2 3p^6 3d^{6.5} 4s^1 4p^0$ and $2s^2 2p^4$ for Fe and O, respectively. Such potentials were generated, tested, and previously used, e.g., in Ref. [46]. A kinetic-energy cutoff of 50 Ry for wave functions and 500 Ry for spin-charge density and potentials were used. In all cases, the atomic orbitals were used to construct occupation matrices and projectors in the LDA+U scheme.

Three $B1$ structures and two $B8$ structures were considered in the present calculations, that is rhombohedra $B1$ ($rB1$, space group $R\bar{3}m$), monoclinic $B1$ ($mB1$, space group $C2/m$), cubic $B1$ ($cB1$, space group $Fm\bar{3}m$), inverse $B8$ ($iB8$, space group $P6_3/mmc$), and normal $B8$ (nB8). The structures are plotted in Fig. 1. A $6 \times 6 \times 6$ **k**-point mesh was used for Brillouin-zone integration for all structures, which was sufficient to achieve a convergence of 1 meV/atom in the total energy. The convergence thresholds are 0.01 eV/Å for the atomic force, 0.5 kbar for the pressure, and 1×10^{-5} eV for the total energy.

The Hubbard correction [18] was applied to Fe-3d states. The total energy E in the LDA+U functional with the simplified formulation of Dudarev *et al.* [42] is written as

$$E = E_{\mathrm{LDA}} + \frac{U}{2} \sum_{I,\sigma} \mathrm{Tr}[\boldsymbol{n}^{I,\sigma}(1 - \boldsymbol{n}^{I,\sigma})], \qquad (1)$$

where E_{LDA} is the LDA ground-state energy and $\boldsymbol{n}^{I,\sigma}$ is the occupation matrix of the atomic site I with spin σ. The Hubbard parameter U was computed using DFPT [27] implemented in the QUANTUM ESPRESSO code [43,44]. The convergence threshold for the response function is 1×10^{-10} Ry.

Here, we automated an iterative scheme to obtain a self-consistent U_{sc} parameter while simultaneously optimizing the structure and desired spin state: Starting from an empirical U of 4.3 eV, the energies of all possible occupation matrices for a spin state were computed. There are five possible occupation matrices corresponding to the HS state of ferrous iron with $3d^6$ configuration ($S = 2$), while there are ten possibilities for

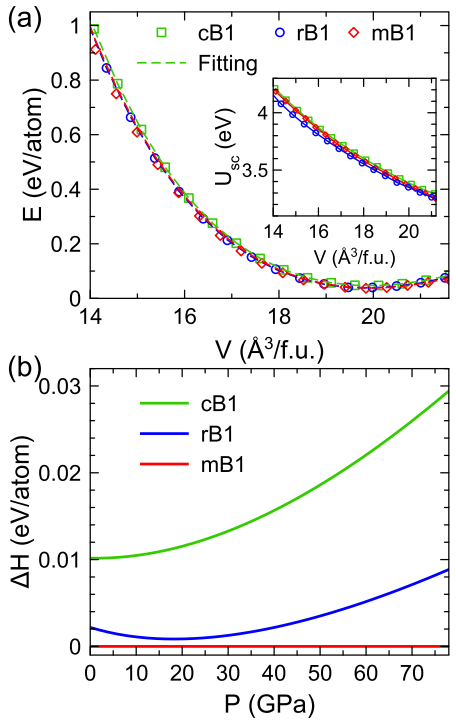

FIG. 2. (a) Relative energies of the three $B1$ phases. The dashed line gives results fitted with the third-order Birch-Murnaghan equation of state. The inset shows the self-consistent Hubbard parameters as a function of the volume for the three phases. (b) Relative enthalpies of the three $mB1$ phases. These results are from static calculations.

the LS state ($S = 0$). The electronic configuration, i.e., occupation matrix, with the lowest energy, was selected for further structural optimization of both lattice parameters and atomic positions. Then the U parameter is recalculated for further structural optimization. The process continued until mutual convergence of structure and U is achieved for a convergence threshold of 0.01 eV for the U parameter and the convergence criteria mentioned above for structural optimizations.

IV. RESULTS AND DISCUSSION

A. $B1$ phases

Using the LDA + U_{sc} scheme, we first investigate FeO with the $cB1$, $rB1$, and $mB1$ structures. The lattices and antiferromagnetic configurations of $rB1$ and $mB1$ phases are shown in Figs. 1(a) and 1(b), respectively. The cubic structure is represented by the rhombohedral lattice with fixed lattice angles [14]. The $rB1$ and $mB1$ structures were fully relaxed for the lattice parameters at each volume. After relaxation, the structures were symmetrized with a tight tolerance of 0.01 Å using the FINDSYM software [47], which confirms no symmetry change happens during the relaxation. $cB1$ lattice has no degree of freedom to be relaxed, so only self-consistent calculations are performed to obtain energy. Figure 2(a) shows the volume-dependent energy and self-consistent Hubbard parameters for three $B1$ phases. The obtained Hubbard parameters are very close among the three phases but show a strong dependence on the pressure. The energy-volume data were fitted by the third-order Birch-Murnaghan (BM) equation of state (EoS). The enthalpies were obtained from the static compression curves fitted to the BM-EoS and are shown in Fig. 2(b). At $P = 0$ GPa, the $mB1$ structure is only 2.2 meV/atom (equivalent to ∼25 K) lower than the $rB1$ structure. This is consistent with the fact that the $mB1$ phase was only observed at very low temperatures, $T = 10$ K [31]. The $mB1$ phase has lower enthalpy than the $cB1$ and $rB1$ phases at all pressures in this static calculation. Vibrational effects may change this result at some pressure and temperature, but this effect was not investigated here. EoS parameters and bond lengths of the $mB1$ phase at the equilibrium volume V_0 are shown in Table I. The equilibrium volume and distorted bond lengths show excellent agreement with experimental data [31]. It is even closer to experiments compared to the hybrid functional results obtained with Becke-3 Perdew-Wang (B3PW91) [48]. Therefore, the calculation with a self-consistent Hubbard parameter seems more predictive than the one with constant "magic number" 4.2 eV used in previous calculations [48]. This result may change somewhat after the inclusion of vibrational effects, but it is clear the self-consistent scheme is necessary to obtain a Hubbard parameter for a predictive DFT+U calculation.

Figure 3 shows the compression curves of the $B1$ phases. The three polytypes ($cB1$, $rB1$, and $mB1$) show very similar compressive behavior. Still, it can be noticed that structures with more degrees of freedom (dg) to relax ($dg^{mB1} > dg^{rB1} > dg^{cB1}$) are more compressive, i.e., $\beta^{mB1} > \beta^{rB1} > \beta^{cB1}$, where β is the compressibility. Comparing with the results of a previous hybrid functional calculation (B3PW91) [48], results are consistent except that the B3PW91 results deviated from ours in the range of 5–20 GPa. B3PW91 results *do not* fit the BM-EoS well.

Next, we compare our $B1$ compression curve calculations with experimental data from a few different experiments [1,49,50], to the best of our knowledge. This comparison

TABLE I. Comparison of structural information of the $mB1$ with previous results. V_0 is the equilibrium volume at $P = 0$ GPa. K_0 and K_0' are the bulk modulus and the derivative of bulk modulus, respectively. Calculations are all static.

Methods	V_0(Å^3/f.u.)	K_0 (GPa)	K_0'	Octahedron distortion	
				Long bond (Å)	Short bond (Å)
Experiment $Fe_{0.99}O$ at 10 K [31]	20.090			2.165	2.154
LDA + U_{sc}	19.915	188.1	4.01	2.171	2.144
B3PW91 [48]	19.804	167.5	3.70	2.176	2.145

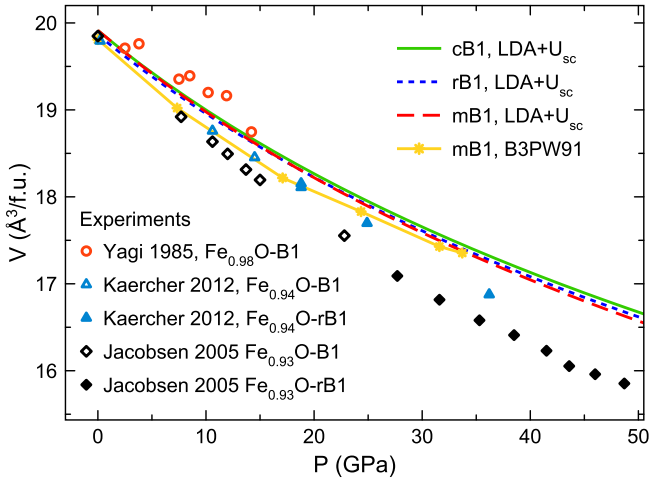

FIG. 3. Pressure-volume curves of $B1$ phases from calculations and experiments. The results of the B3PW91 calculation are from Ref. [48]. Experiments were performed at room temperature by Yagi *et al.* [1], Jacobsen *et al.* [49], and Kaercher *et al.* [50].

clearly shows that the compressive behavior of FeO depends quite strongly on this compound stoichiometry. Iron vacancies are common in experiments because Fe is a multivalent ion and frequently exists in the ferric form (Fe^{3+}). The higher the iron vacancy concentration, the higher the compressibility. The present calculations have no vacancies. Therefore, they show smaller compressibility than the experimental data. Despite having no vacancies, our volumes are smaller than those reported for $Fe_{0.98}O$. The static nature of our results causes this. The inclusion of vibrational effects would likely improve agreement between theoretical and experimental data at 300 K [51]. Considering these two effects, i.e., stoichiometry

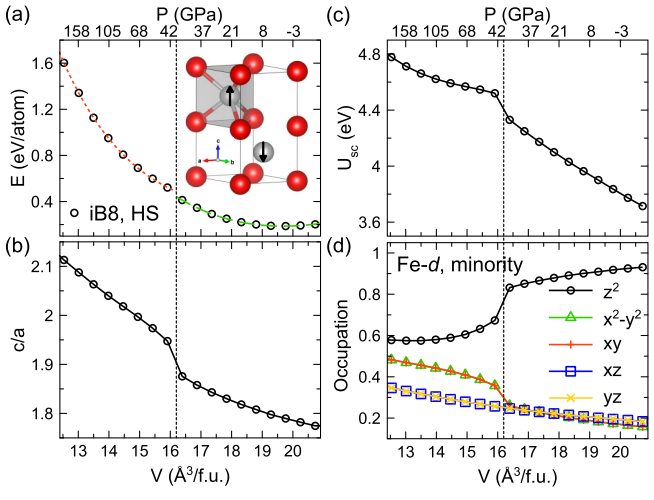

FIG. 4. (a) The energy-volume curves for the $iB8$ phase in the HS state. The red dotted line and green dashed lines are the BM-EoS fittings for small volume and large volume results, respectively. The inset shows the atomic structure of the $iB8$-HS phase. Gray and red spheres are iron and oxygen, respectively. (b) The c/a ratio and (c) the self-consistent Hubbard parameters vs volume. (d) Minority electron d-orbital occupancies vs volume. The vertical lines indicate the discontinuities.

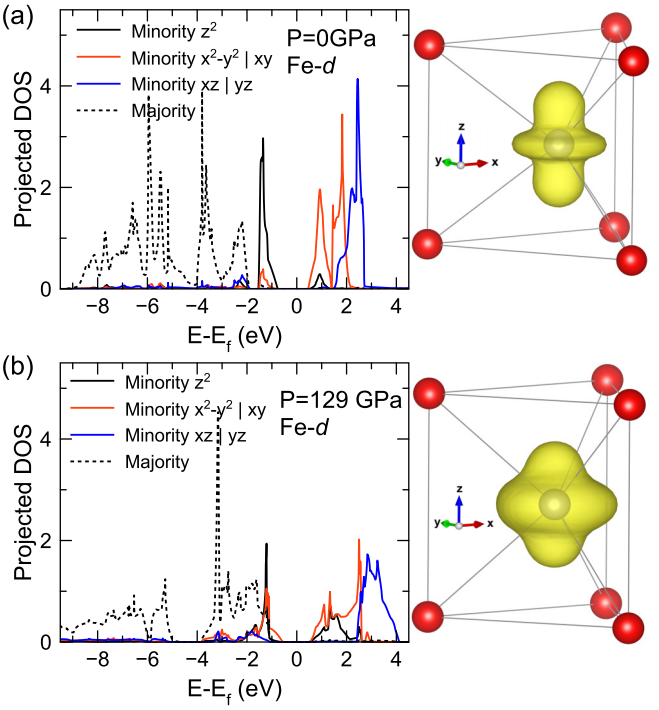

FIG. 5. Electronic density of state of Fe d orbitals in the $iB8$-HS at (a) 0 GPa and (b) 129 GPa. The right panel shows the occupied Fe-d minority orbital. The isosurface threshold values are the same in (a) and (b).

difference and vibrational effects, the current agreement between theoretical results and room-temperature experimental data can be regarded as excellent. Therefore, LDA + U_{sc} can indeed well describe the structural properties of insulating B1 phases.

B. $B8$ phases

Figure 4 shows the LDA + U_{sc} results for the $iB8$ HS state ($S = 2$). The antiferromagnetic configuration consists of alternating up and down spins along the c direction. The energy-volume curve in Fig. 4(a) shows an unexpected discontinuity at 16.2 Å^3/f.u. near 40 GPa. It requires two BM-EoS fittings, one for the high-pressure and one for the low-pressure results. The c/a ratio and the computed self-consistent Hubbard parameter also show a consistent discontinuity at the same volume (pressure) in Figs. 4(b) and 4(c). The origin of this behavior can be tracked to the orbital occupancy of the minority d electron in Fe^{2+} in the HS state. In the $iB8$ HS structure the majority spin-up bands are full, so only one electron enters in the spin-down bands ($d^5_\uparrow d^1_\downarrow$ electronic configuration). The projected atomic orbital occupancies for the minority electron are plotted vs volume in Fig. 4(d). At large volumes, the occupied state is mainly a z^2-type orbital (short for $3z^2 - r^2$), but the z^2 orbital occupancy decreases under compression. Note that the z axis is aligned along the crystal c axis. For $V \leqslant 16.2$ Å^3/f.u. (∼40 GPa), the occupied d band shows a strongly mixed $z^2/x^2 - y^2/xy$ character. To clarify this situation, we show in Fig. 5 the projected electronic density of state for Fe d orbitals in the $iB8$-HS phase at

low and high pressures. One can see a greater orbital mixing at higher pressures by comparing Figs. 5(a) and 5(b). The shapes of the occupied localized orbitals are also shown in Fig. 5, indicating that the minority electronic density shifts to the *x*-*y* plane, and the *c*-axis compressibility increases after that. The band gap of ∼1.0 eV is essentially pressure independent.

This electronic transition in the *iB*8-HS phase has structural effects, but it is a metastable transition, i.e., the stable phase at ∼40 GPa is the *mB*1 phase. Nevertheless, this type of electronic transition in iron is not uncommon. For example, Mössbauer spectroscopy detected the increased presence of a second type of ferrous iron with higher quadrupole splitting (3.5 mm/s) in $(Mg, Fe)SiO_3$-perovskite, i.e., bridgmanite, starting at 30 GPa and ending at 60 GPa [52]. Such change was attributed to an HS to intermediate spin state ($S = 1$) change, which happens continuously with pressure. It was later shown that such state change consists of the change of orbital occupancy of the minority *d*-electron [53], which is also accompanied by a change of the compressibility of bridgmanite [54]. The total spin, $S = 2$, was not altered throughout this electronic transition [55].

To compare the relative stability of the B1 and B8 phases, LDA + U_{sc} calculations were performed for *nB*8, *iB*8, and *B*1 phases in both HS and LS states. Because the ferromagnetic configuration shows higher energy than the antiferromagnetic configurations at all volumes, only antiferromagnetic configurations are reported here. Because the *iB*8-LS phase had high energy and is mechanically unstable, consistent with a previous finding [26], the *iB*8-LS phase is omitted here. By checking the symmetry of the relaxed structures, we find the *rB*1-LS and *mB*1-LS phases spontaneously transform to the *cB*1-LS structure, so there are no *rB*1-LS or *mB*1-LS states. More importantly, these *B*1-LS phases transform to the *nB*8-LS when volumes are smaller than 12.0 $Å^3$/f.u. (i.e., ∼160 GPa). All the LDA + U_{sc} results for *B*1 and *B*8 phases are shown in Fig. 6.

The self-consistent Hubbard parameters are shown in Fig. 6(b) and display strong dependences on pressure, structure, and spin states. LS states systematically have larger Hubbard parameters than HS states, regardless of structure. Figure 6(c) shows average Fe–O bond lengths versus pressure. They are almost indistinguishable in *mB*1-HS, *cB*1-HS, *rB*1-HS, and *nB*8-HS phases and the *cB*1-LS and *nB*8-LS phases. Iron in these phases is all octahedrally coordinated (see Fig. 1). The pressure dependence of the average FeO bond lengths in *iB*8-HS is different from those of other phases. In this phase, the iron coordination polyhedron is a triangular prism. Therefore, phases with iron with the same coordination polyhedron and spin state have almost indistinguishable Fe–O bond lengths at the same pressure.

The relative stability of these phases is shown in Fig. 6(d). The *mB*1 phase is the most stable up to 110 GPa at $T = 0$ K. Because only the *rB*1 phase (stable at room temperature) was reported in the previous high-pressure experiments, we focus on the phase transitions from the latter. The current LDA + U_{sc} calculations produce two phase transitions: *rB*1-HS to *iB*8-HS at 105 GPa and *iB*8-HS to *nB*8-LS at 245 GPa, which are all insulating phases. The first transition from *rB*1-HS to *iB*8-HS is very consistent with the experimental transition pressure of ∼105 GPa at room temperature [2,30,32]. However, the second transition from *iB*8-HS to *nB*8-LS happens at a significantly larger pressure than the experimental transition pressure of 120 GPa [39]. By examining the electronic density of state shown in Fig. 7(a), we find this *nB*8-LS state to be insulating with a band gap of ∼0.8 eV, which contrasts with the metallic *nB*8-LS phase obtained experimentally. The current LDA + U_{sc} scheme mainly promotes the insulating state by penalizing the metallic state with increasing U_{sc} at higher pressures. To evade this problem, after obtaining U_{sc}, we continue calculations on this phase using the Mermin functional [56,57], with orbitals occupancies given by the Fermi-Dirac distribution and electronic entropy contribution included in the total "free-energy" calculation. We test the outcome of this strategy for variable "electronic temperature," T_{el}. As shown in Fig. 7, by increasing T_{el}, the Fermi level gradually shifts to the conduction band, and the transition pressure from *iB*8-HS to *nB*8-LS decreases. With $T_{el} \sim 7000$ K, the *nB*8-LS phase becomes a metal. The *iB*8-HS to *nB*8-LS transition pressure is also lowered to ∼120 GPa, in agreement with the experimental value of 120 GPa. The metallization of the *nB*8-LS phase and the *iB*8-HS to *nB*8-LS transition pressure can be controlled by the magnitude of T_{el} and the value of the Hubbard parameter, though freely manipulating the latter is not under consideration here. This artificially large T_{el} and its codependence on the Hubbard *U* value points to the necessity to render the DFT + U_{sc} scheme more flexible to improve its description of metallic ground states.

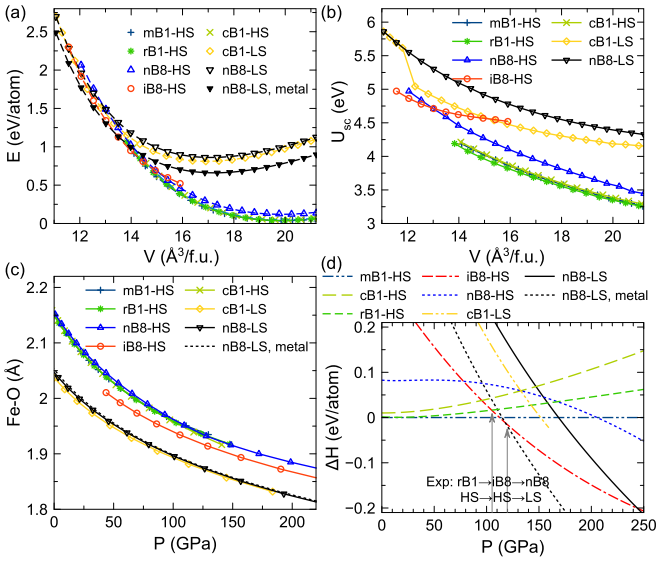

FIG. 6. (a) Energy-volume relation for relevant *B*1 and *B*8 phases. The curves of *mB*1-HS, *cB*1-HS, and *rB*1-HS are almost overlapped on this scale. (b) Self-consistent Hubbard parameter vs volume for the same phases. (c) Average Fe–O bond lengths vs pressure. (d) Relative enthalpies using the data of *mB*1-HS phase as the reference. Arrows indicate experimental transition pressures of *rB*1-HS to *iB*8-HS to *nB*8-LS. The "*nB*8-LS, metal" indicates the one using Mermin functional with $T_{el} = 7000$ K.

The structures of *iB*8-HS and *nB*8-LS are also compared with experimental data in Fig. 8. Calculated volume and c/a ratio for the *iB*8-HS state agree well with the experimental data obtained at room temperature [39]. Because the *iB*8-HS was found experimentally to be insulating; the current

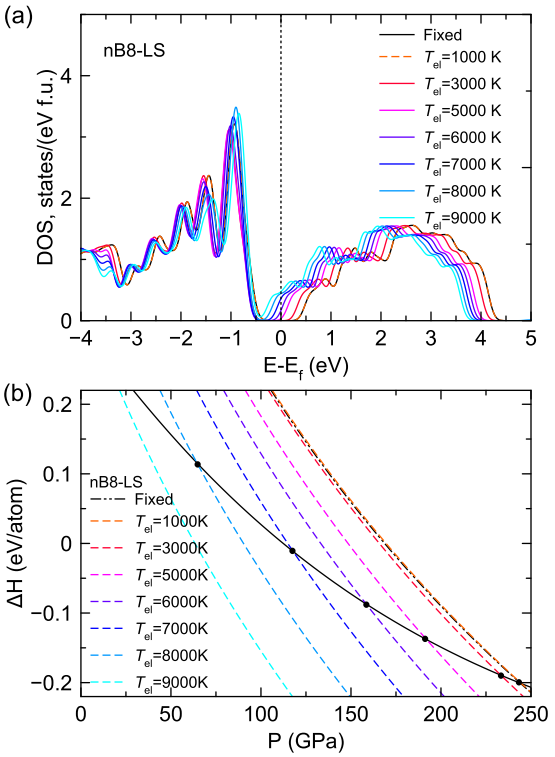

FIG. 7. (a) The density of state of *nB*8-LS at 110 GPa using different occupation schemes. "Fixed" corresponds to the fixed-occupation scheme for the insulating state. The T_{el} corresponds to the broadening in the Fermi-Dirac smearing. (b) Relative enthalpies of *iB*8-HS and *nB*8-LS with smearing. The enthalpy of *mB*1-HS is used as the reference. The dots indicate the transition pressure.

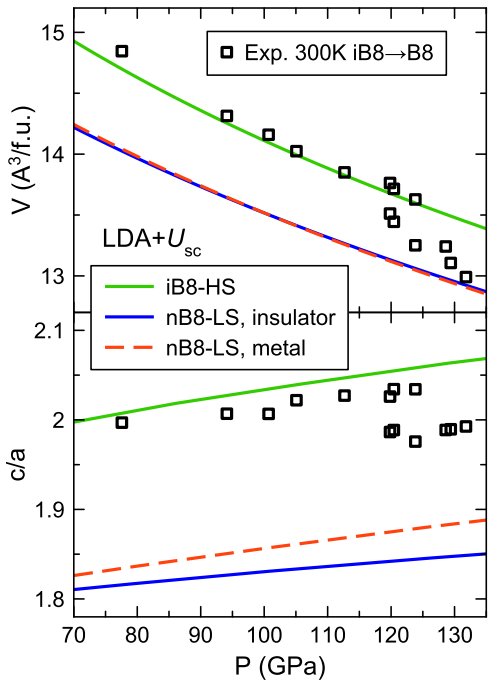

FIG. 8. The volume and c/a ratio as a function of pressure for *iB*8-HS and *nB*8-LS phases. The experimental data include both *iB*8 and *nB*8 data with a transition pressure at 120 GPa [39].

LDA + U_{sc} scheme indeed describes its electronic and structural characters quite well. However, the insulating *nB*8-LS phase shows a significant deviation from experimental values in the c/a ratio. Treating the system as metallic by using the Mermin functional with an electronic temperature T_{el}, the c/a ratio gets closer to the experimental values.

The current calculation does not include spin-orbit coupling (SOC) effect because it is believed to be insignificant in the FeO system [13]. To confirm this idea, we examine the SOC effect on the transition pressure from *rB*1-HS to *iB*8-HS in the Supplemental Material [58]. We find that SOC increases the total energy of both *rB*1-HS and *iB*8-HS phases by ∼0.04 eV/atom almost uniformly in the volume range explored. Therefore, it does not change the transition pressure noticeably.

V. CONCLUSION

In summary, we have shown that with a careful determination of the Hubbard parameter, LDA + U_{sc} can well describe phase relations among and compression curves of *insulating* FeO phases. The self-consistent Hubbard parameter U_{sc} depends strongly on pressure, structure, and spin state, varying typically by 1–3 eV, as shown in Fig. 6. Therefore, DFT+U calculations with constant or artificially tuned U values may not be able to capture structural and electronic properties fully. For *B*1 phases, current calculations confirm the *mB*1 phase should be the ground state at $T = 0$ K, while the *rB*1 phase shows similar enthalpy to that of the *mB*1 phase. Therefore, the *mB*1 phase could only be observed experimentally at low temperatures [31]. We also found a metastable electronic transition in the *iB*8-HS phase at ∼40 GPa. This transition consists of a change in orbital occupancy of the minority d electron, a phenomenon similar to that observed in ferrous iron in (Mg, Fe)SiO_3 between 30 and 60 GPa [52,53]. The zero-temperature phase boundary between rB1-HS and *iB*8-HS is 105 GPa, which is very consistent with the room-temperature observation at 105 GPa [30,32]. The equilibrium volume of *mB*1-HS, the compression curve of B1-HS and *iB*8-HS agrees very well with experimental measurements. The only discrepancy between current calculations and experiments is on the *nB*8-LS state that overestimates the transition pressure and underestimates the structural c/a ratios compared to experiments. This is because LDA + U_{sc} produces an insulating state for *nB*8 while it should be metallic. By using the Mermin functional *a posteriori*, i.e., without further changing U, and an artificially large electronic temperature $T_{el} \sim 7000$ K, the LDA+U calculation produces a metallic state, improves structural properties, and produces an *iB*8-HS to *nB*8-LS transition pressure in good agreement with experiments. All these properties can also be modified by changing the Hubbard parameter. This artificially large T_{el} and its codependence on the Hubbard U value points to the type of modification necessary in the DFT + U_{sc} scheme to address the metallic state that includes electronic entropy contributions in the electronic free energy.

ACKNOWLEDGMENTS

The authors thank Y. Yao, V. Antropov, and K.-M. Ho for helpful discussion. This work was funded in part by

National Science Foundation Award No. EAR-1918126 (Y.S.) and in part by the US Department of Energy Award No. DESC0019759 (R.M.W.). This work used the Extreme Science and Engineering Discovery Environment (XSEDE), USA, which was supported by the National Science Foundation, USA Grant No. ACI-1548562. The authors acknowledge the Texas Advanced Computing Center (TACC) at The University of Texas at Austin for providing Stampede2 HPC resources that have contributed to the research results reported within this paper.

[1] T. Yagi, T. Suzuki, and S. I. Akimoto, J. Geophys. Res. **90**, 8784 (1985).
[2] Y. Fei and H. K. Mao, Science **266**, 1678 (1994).
[3] R. E. Cohen, I. I. Mazin, and D. G. Isaak, Science **275**, 654 (1997).
[4] B. Lavina, P. Dera, E. Kim, Y. Meng, R. T. Downs, P. F. Weck, S. R. Sutton, and Y. Zhao, Proc. Natl. Acad. Sci. **108**, 17281 (2011).
[5] B. Lavina and Y. Meng, Sci. Adv. **1**, e1400260 (2015).
[6] Q. Hu, D. Y. Kim, W. Yang, L. Yang, Y. Meng, L. Zhang, and H.-K. Mao, Nature (London) **534**, 241 (2016).
[7] K. Terakura, T. Oguchi, A. R. Williams, and J. Kübler, Phys. Rev. B **30**, 4734 (1984).
[8] A. R. Oganov, Y. Ma, A. O. Lyakhov, M. Valle, and C. Gatti, Rev. Mineral. Geochem. **71**, 271 (2010).
[9] S. Q. Wu, M. Ji, C. Z. Wang, M. C. Nguyen, X. Zhao, K. Umemoto, R. M. Wentzcovitch, and K. M. Ho, J. Phys.: Condens. Matter **26**, 035402 (2014).
[10] A. R. Oganov, Y. Ma, C. W. Glass, and M. Valle, Psi-k Newsl. **84**, 142 (2007).
[11] G. L. Weerasinghe, C. J. Pickard, and R. J. Needs, J. Phys.: Condens. Matter **27**, 455501 (2015).
[12] A. R. Oganov, C. J. Pickard, Q. Zhu, and R. J. Needs, Nat. Rev. Mater. **4**, 331 (2019).
[13] I. I. Mazin and V. I. Anisimov, Phys. Rev. B **55**, 12822 (1997).
[14] M. Cococcioni and S. de Gironcoli, Phys. Rev. B **71**, 035105 (2005).
[15] A. Georges, G. Kotliar, W. Krauth, and M. J. Rozenberg, Rev. Mod. Phys. **68**, 13 (1996).
[16] A. O. Shorikov, Z. V. Pchelkina, V. I. Anisimov, S. L. Skornyakov, and M. A. Korotin, Phys. Rev. B **82**, 195101 (2010).
[17] N. Lanatà, T.-H. Lee, Y.-X. Yao, V. Stevanović, and V. Dobrosavljević, Npj Comput. Mater. **5**, 30 (2019).
[18] V. I. Anisimov, J. Zaanen, and O. K. Andersen, Phys. Rev. B **44**, 943 (1991).
[19] H. J. Kulik, M. Cococcioni, D. A. Scherlis, and N. Marzari, Phys. Rev. Lett. **97**, 103001 (2006).
[20] H. Hsu, K. Umemoto, Z. Wu, and R. M. Wentzcovitch, Rev. Mineral. Geochem. **71**, 169 (2010).
[21] T. Tsuchiya, R. M. Wentzcovitch, C. R. S. da Silva, and S. de Gironcoli, Phys. Rev. Lett. **96**, 198501 (2006).
[22] R. M. Wentzcovitch, J. F. Justo, Z. Wu, C. R. S. da Silva, D. A. Yuen, and D. Kohlstedt, Proc. Natl. Acad. Sci. **106**, 8447 (2009).
[23] M. Cococcioni and N. Marzari, Phys. Rev. Mater. **3**, 033801 (2019).
[24] A. Floris, I. Timrov, B. Himmetoglu, N. Marzari, S. deGironcoli, and M. Cococcioni, Phys. Rev. B **101**, 064305 (2020).
[25] S. A. Gramsch, R. E. Cohen, and S. Y. Savrasov, Am. Mineral. **88**, 257 (2003).
[26] K. Persson, A. Bengtson, G. Ceder, and D. Morgan, Geophys. Res. Lett. **33**, L16306 (2006).
[27] I. Timrov, N. Marzari, and M. Cococcioni, Phys. Rev. B **98**, 085127 (2018).
[28] M. Murakami, K. Hirose, S. Ono, T. Tsuchiya, M. Isshiki, and T. Watanuki, Phys. Earth Planet. Inter. **146**, 273 (2004).
[29] K. Ohta, R. E. Cohen, K. Hirose, K. Haule, K. Shimizu, and Y. Ohishi, Phys. Rev. Lett. **108**, 026403 (2012).
[30] T. Irifune and T. Tsuchiya, *Phase Transitions and Mineralogy of the Lower Mantle* (Elsevier BV, Amsterdam, 2015).
[31] H. Fjellvag, B. C. Hauback, T. Vogt, and S. Stolen, Am. Mineral. **87**, 347 (2002).
[32] H. Ozawa, K. Hirose, S. Tateno, N. Sata, and Y. Ohishi, Phys. Earth Planet. Inter. **179**, 157 (2010).
[33] I. I. Mazin, Yingwei Fei, R. Downs, and R. Cohen, Am. Mineral. **83**, 451 (1998).
[34] Z. Fang, K. Terakura, H. Sawada, T. Miyazaki, and I. Solovyev, Phys. Rev. Lett. **81**, 1027 (1998).
[35] M. P. Pasternak, R. D. Taylor, R. Jeanloz, X. Li, J. H. Nguyen, and C. A. Mc Cammon, Phys. Rev. Lett. **79**, 5046 (1997).
[36] J. Badro, V. V. Struzhkin, J. Shu, R. J. Hemley, H. K. Mao, C. C. Kao, J. P. Rueff, and G. Shen, Phys. Rev. Lett. **83**, 4101 (1999).
[37] A. Mattila, J. P. Rueff, J. Badro, G. Vankó, and A. Shukla, Phys. Rev. Lett. **98**, 196404 (2007).
[38] K. Ohta, K. Hirose, K. Shimizu, and Y. Ohishi, Phys. Rev. B **82**, 174120 (2010).
[39] H. Ozawa, K. Hirose, K. Ohta, H. Ishii, N. Hiraoka, Y. Ohishi, and Y. Seto, Phys. Rev. B **84**, 134417 (2011).
[40] D. M. Sherman and H. J. F. Jansen, Geophys. Res. Lett. **22**, 1001 (1995).
[41] I. Leonov, Phys. Rev. B **92**, 085142 (2015).
[42] S. L. Dudarev, G. A. Botton, S. Y. Savrasov, C. J. Humphreys, and A. P. Sutton, Phys. Rev. B **57**, 1505 (1998).
[43] P. Giannozzi, S. Baroni, N. Bonini, M. Calandra, R. Car, C. Cavazzoni, D. Ceresoli, G. L. Chiarotti, M. Cococcioni, I. Dabo, A. Dal Corso, S. de Gironcoli, S. Fabris, G. Fratesi, R. Gebauer, U. Gerstmann, C. Gougoussis, A. Kokalj, M. Lazzeri, and L. Martin-Samos *et al.*, J. Phys.: Condens. Matter **21**, 395502 (2009).
[44] P. Giannozzi, O. Andreussi, T. Brumme, O. Bunau, M. B. Nardelli, M. Calandra, R. Car, C. Cavazzoni, D. Ceresoli, and M. Cococcioni *et al.*, J. Phys.: Condens. Matter **29**, 465901 (2017).
[45] D. Vanderbilt, Phys. Rev. B **41**, 7892 (1990).
[46] K. Umemoto, R. M. Wentzcovitch, Y. G. Yu, and R. Requist, Earth Planet. Sci. Lett. **276**, 198 (2008).
[47] H. T. Stokes and D. M. Hatch, J. Appl. Crystallogr. **38**, 237 (2005).

[48] T. Eom, H. K. Lim, W. A. Goddard, and H. Kim, J. Phys. Chem. C **119**, 556 (2015).
[49] S. D. Jacobsen, J. F. Lin, R. J. Angel, G. Shen, V. B. Prakapenka, P. Dera, H. K. Mao, and R. J. Hemley, J. Synchrotron Radiat. **12**, 577 (2005).
[50] P. Kaercher, S. Speziale, L. Miyagi, W. Kanitpanyacharoen, and H. R. Wenk, Phys. Chem. Miner. **39**, 613 (2012).
[51] R. M. Wentzcovitch, Y. G. Yu, and Z. Wu, Rev. Mineral. Geochem. **71**, 59 (2010).
[52] C. McCammon, I. Kantor, O. Narygina, J. Rouquette, U. Ponkratz, I. Sergueev, M. Mezouar, V. Prakapenka, and L. Dubrovinsky, Nat. Geosci. **1**, 684 (2008).
[53] H. Hsu, K. Umemoto, P. Blaha, and R. M. Wentzcovitch, Earth Planet. Sci. Lett. **294**, 19 (2010).
[54] G. Shukla, Z. Wu, H. Hsu, A. Floris, M. Cococcioni, and R. M. Wentzcovitch, Geophys. Res. Lett. **42**, 1741 (2015).
[55] H. Hsu and R. M. Wentzcovitch, Phys. Rev. B **90**, 195205 (2014).
[56] N. D. Mermin, Phys. Rev. **137**, A1441 (1965).
[57] R. M. Wentzcovitch, J. L. Martins, and P. B. Allen, Phys. Rev. B **45**, 11372 (1992).
[58] See Supplemental Material at http://link.aps.org/supplemental/10.1103/PhysRevMaterials.4.063605 for spin-orbital coupling calculations, which includes Refs. [59,60].
[59] A. I. Liechtenstein, V. I. Anisimov, and J. Zaanen, Phys. Rev. B **52**, R5467 (1995).
[60] S. L. Dudarev, P. Liu, D. A. Andersson, C. R. Stanek, T. Ozaki, and C. Franchini, Phys. Rev. Mater. **3**, 083802 (2019).

Supplemental Material for "LDA+$U_{\rm sc}$ calculations of phase relations in FeO"

Yang Sun,[1] Matteo Cococcioni,[2] and Renata M. Wentzcovith[1,3,4]

[1] *Department of Applied Physics and Applied Mathematics, Columbia University, New York, NY, 10027, USA*
[2] *Department of physics, University of Pavia, 27100 Pavia, Italy*
[3] *Department of Earth and Environmental Sciences, Columbia University, New York, NY, 10027, USA*
[4] *Lamont–Doherty Earth Observatory, Columbia University, Palisades, NY, 10964, USA*

Here, we examine the impact of the spin-orbital coupling (SOC) on the rB1-HS to iB8-HS transition pressure. The SOC calculations are performed with a rotationally invariant form of LSDA+U+J functional [1]. The parameter J is fixed at $J_c = 0.9$ and $U = U_{sc} + J_c$, where U_{sc} is obtained from self-consistent calculations with the simplified formulation of Dudarev *et al.* [2], as described in the main text. The fully relativistic pseudopotential is employed for the SOC calculations.

Figure S1(a) shows that the inclusion of SOC systematically increases the energy ~ 0.04 eV/atom, with a small dependence on pressure and phase. Because the SOC effect is similar on both rB1-HS and iB8-HS phases, it only changes the transition pressure ~ 2GPa of ~ 110GPa, as shown in Fig. S1(b). Therefore, while SOC can indeed affect the results of total energy calculation, the impact on transition pressure is small.

Due to the change of pseudopotentials the self-consistent $U_{\rm sc}$ is recalculated for both phases. The new values are provided in Fig. S1(c). The current SOC calculation is not fully self consistent because of the presumed J value. A more sophisticated calculation may be carried out using a recently developed noncollinear LSDA+U technique [3].

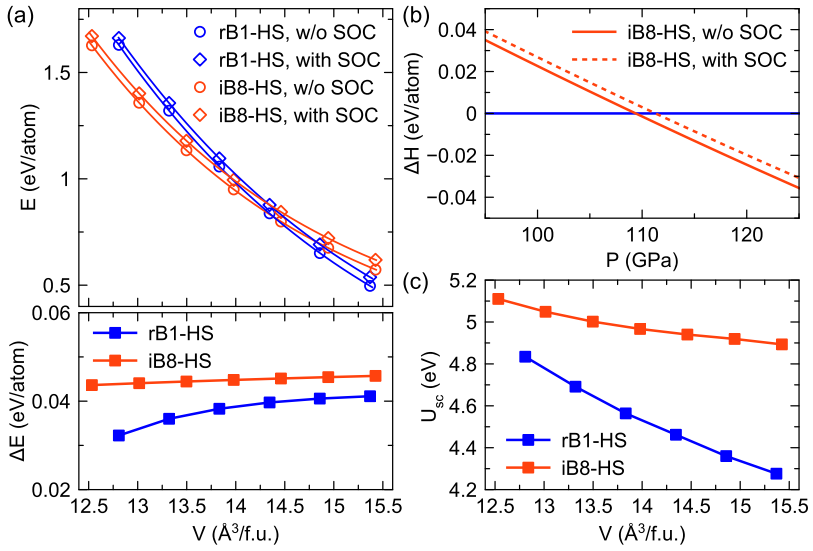

FIG. 1. (a) The upper panel shows the Energy-volume relation for rB1-HS and iB8-HS phases with and without spin-orbital coupling. The solid lines are the fitting results with the third-order Birch-Murnaghan equation of state. The lower panel shows the energy difference caused by the inclusion of SOC, i.e. $\Delta E = E_{SOC} - E$. (b) Relative enthalpies using the data of rB1-HS phase as the reference. (c) The self-consistent U_{sc} value.

[1] A. I. Liechtenstein, V. I. Anisimov, and J. Zaanen, Phys. Rev. B 52, R5467 (1995).
[2] S. L. Dudarev, G. A. Botton, S. Y. Savrasov, C. J. Humphreys, and A. P. Sutton, Phys. Rev. B 57, 1505 (1998).
[3] S. L. Dudarev, P. Liu, D. A. Andersson, C. R. Stanek, T. Ozaki, and C. Franchini, Phys. Rev. Mater. 3, 083802 (2019).